nature energy

ARTICLES

https://doi.org/10.1038/s41560-020-0634-5

Check for updates

Molecular design for electrolyte solvents enabling energy-dense and long-cycling lithium metal batteries

Zhiao Yu[1,2,6], Hansen Wang[3,6], Xian Kong[1], William Huang[3], Yuchi Tsao[1,2,3], David G. Mackanic[1], Kecheng Wang[3], Xinchang Wang[4], Wenxiao Huang[3], Snehashis Choudhury[1], Yu Zheng[1,2], Chibueze V. Amanchukwu[1], Samantha T. Hung[2], Yuting Ma[1], Eder G. Lomeli[3], Jian Qin[1], Yi Cui[3,5]✉ and Zhenan Bao[1]✉

Electrolyte engineering is critical for developing Li metal batteries. While recent works improved Li metal cyclability, a methodology for rational electrolyte design remains lacking. Herein, we propose a design strategy for electrolytes that enable anode-free Li metal batteries with single-solvent single-salt formations at standard concentrations. Rational incorporation of $-CF_2-$ units yields fluorinated 1,4-dimethoxylbutane as the electrolyte solvent. Paired with 1 M lithium bis(fluorosulfonyl)imide, this electrolyte possesses unique Li–F binding and high anion/solvent ratio in the solvation sheath, leading to excellent compatibility with both Li metal anodes (Coulombic efficiency ~ 99.52% and fast activation within five cycles) and high-voltage cathodes (~6 V stability). Fifty-µm-thick Li|NMC batteries retain 90% capacity after 420 cycles with an average Coulombic efficiency of 99.98%. Industrial anode-free pouch cells achieve ~325 Wh kg^{-1} single-cell energy density and 80% capacity retention after 100 cycles. Our design concept for electrolytes provides a promising path to high-energy, long-cycling Li metal batteries.

Li-ion batteries have made a great impact on society, recognized recently by the Nobel Prize in Chemistry[1,2]. Following decades of commercialization, Li-ion batteries are rapidly approaching their theoretical limit in energy density, motivating the revival of Li metal chemistry[3–6]. Nevertheless, the implementation of Li metal batteries is plagued by their poor cycle life[4,5]. Uncontrollable side reactions between Li metal and electrolytes form a chemically unstable and mechanically fragile solid–electrolyte interphase (SEI). The SEI easily cracks during cycling, leading to dendritic growth, 'dead Li' formation and irreversible Li inventory loss[4]. Electrolyte engineering tunes both the SEI structure and chemistry, making it a critical and pragmatic approach to enabling Li metal anodes[7,8]. For a promising electrolyte, several key requirements must be simultaneously met[9–11]: (1) consistently high Coulombic efficiency (CE) to minimize Li loss, including in the initial cycles, (2) functionality under lean electrolyte and limited-excess Li conditions for maximum specific energy, (3) oxidative stability towards high-voltage cathodes, (4) reasonably low salt concentration for cost-effectiveness and (5) high boiling point and non-flammability for safety and processability.

Recent works on electrolyte engineering improved the cyclability of Li metal batteries, including salt additive optimization[12], solvent ratio modification[13,14] and liquefied gas electrolyte[15]. In particular, high-concentration electrolytes[16,17] and localized high-concentration electrolytes[11,18–22] were recognized to be the most effective methods. The high-concentration electrolytes successfully reduced the free solvent molecules within the Li^+ solvation structure, leading to a primarily inorganic SEI and better Li cyclability. A whole family of fluorinated diluent molecules were further developed to form localized high-concentration electrolytes, compensating the high viscosity of high-concentration electrolytes. Despite these advances, current electrolyte design methodology is still not ideal. The diluent molecules used in localized high-concentration electrolytes are Li metal compatible yet hardly able to solvate Li^+ ions by themselves. As a consequence, small amounts of unstable solvents (for example sulfolane[19], triethyl phosphate[21] or dimethyl carbonate[22]) are necessary for salt dissolution, reducing but not eliminating undesirable parasitic reactions. These persistent side reactions with the solvent molecules lead to low CE in the initial cycles. Therefore, designing new solvent molecules that are stable towards Li metal while still maintaining the capability of solvating Li^+ is highly desirable.

In this work, fluorinated 1,4-dimethoxylbutane (FDMB, Fig. 1) is synthesized by selectively functionalizing lengthened ether backbones with $-CF_2-$ groups. Our design enables the FDMB molecule to solvate Li^+ ions with a unique Li–F interaction that is beneficial to both Li metal anode compatibility and high-voltage tolerance. Paired with 1 M lithium bis(fluorosulfonyl)imide (LiFSI) in a single-salt, single-solvent formulation, this 1 M LiFSI/FDMB electrolyte not only endows Li metal with an ultrathin SEI (~6 nm) observed by cryogenic transmission electron microscopy (cryo-TEM) and high CE (~99.52%) along with a fast activation process (CE > 99% within five cycles), but also achieves >6 V oxidative stability. The limited-excess Li|NMC (lithium nickel manganese cobalt oxide) full cells retain 90% capacity after 420 cycles with an average CE of 99.98%. Industrial anode-free Cu|NMC811 ($LiNi_{0.8}Mn_{0.1}Co_{0.1}O_2$) pouch cells achieve ~325 Wh kg^{-1} single-cell energy density,

[1]Department of Chemical Engineering, Stanford University, Stanford, CA, USA. [2]Department of Chemistry, Stanford University, Stanford, CA, USA. [3]Department of Materials Science and Engineering, Stanford University, Stanford, CA, USA. [4]School of Electronic Science and Engineering, Xiamen University, Xiamen, Fujian, China. [5]Stanford Institute for Materials and Energy Sciences, SLAC National Accelerator Laboratory, Menlo Park, CA, USA. [6]These authors contributed equally: Zhiao Yu, Hansen Wang. ✉e-mail: yicui@stanford.edu; zbao@stanford.edu

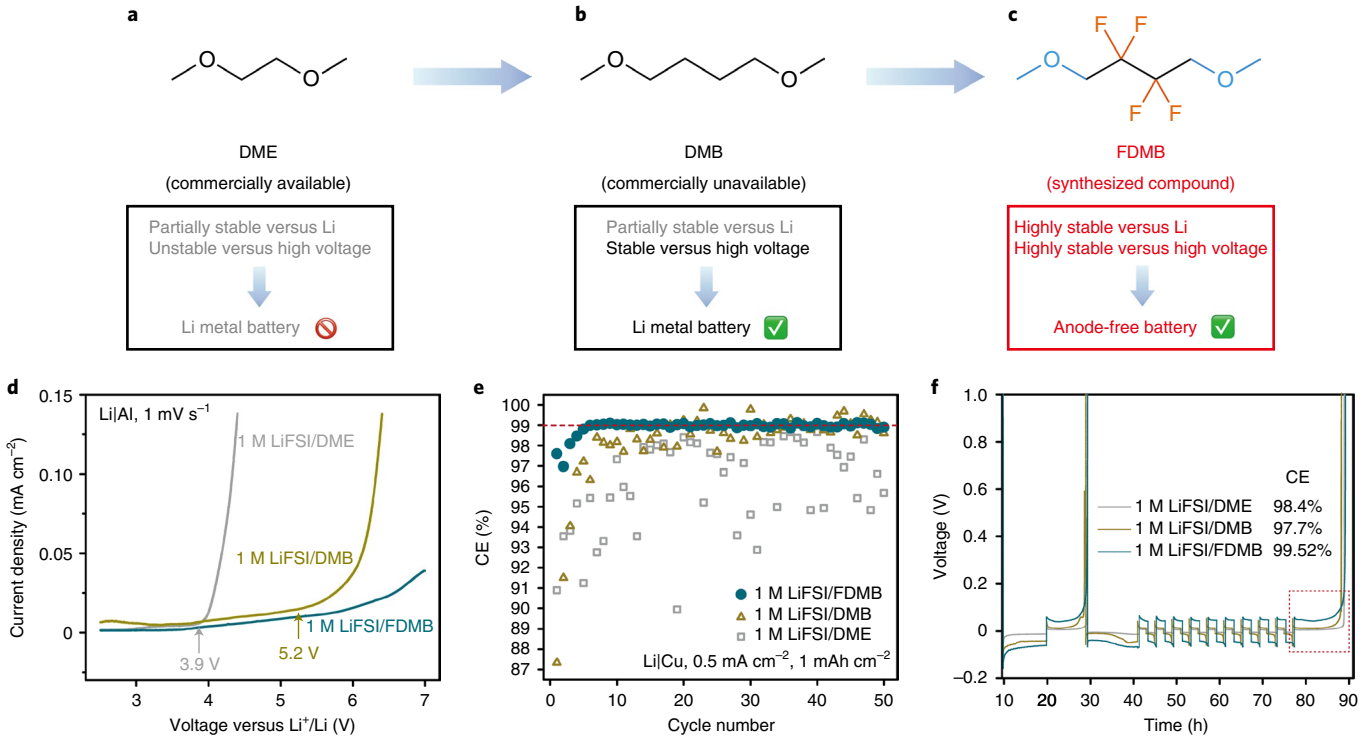

Fig. 1 | Design concepts and electrochemical stability of electrolytes studied in this work. a–c, Design scheme and molecular structures of three liquids studied in this work: DME (**a**), DMB (**b**) and FDMB (**c**). **d**, Oxidation stability of three electrolytes in Li|Al half cells detected by LSV. **e**,**f**, Cycling (**e**) and Aurbach[34] measurement (**f**) of Li metal CE in Li|Cu half cells using different electrolytes. For clarity, only the first 50 cycles of long-term cycling are shown here.

while Cu|NMC532 ($LiNi_{0.5}Mn_{0.3}Co_{0.2}O_2$) ones show a record-high 80% capacity retention after 100 cycles. Furthermore, the 1 M LiFSI/FDMB electrolyte is less flammable than commercial electrolytes and can be synthesized at large scale with low cost. Our electrolyte formulation satisfies the stringent requirements for a practical Li metal battery outlined above.

Molecular design

To target a desired electrolyte solvent molecule, the ether backbone is chosen here due to its ability to solvate Li^+ ions and benefit Li metal anodes[18,23,24]; however, ethers usually show poor oxidation stability[7,18,23–25], which seriously affects the battery performance when high-voltage cathodes are applied. Therefore, we propose two critical design concepts to ensure the oxidative stability as well as the Li cycling efficiency. First, the alkyl chain in the middle of a commonly used ether electrolyte structure, 1,2-dimethoxylethane (DME, Fig. 1a), is lengthened to obtain 1,4-dimethoxylbutane (DMB, Fig. 1b). The motivation is to take advantage of the robustness of a longer alkyl chain[26,27] while still maintaining the ability to solvate Li salt and conduct Li^+ ions. Second, –F groups are introduced to further enlarge the oxidation window and Li metal compatibility[28,29]. Nonetheless, it is known that only when the –F groups are distant from –O– groups can the solvation ability of the ether be maintained[11,18–22]. Hence only the central part of the DMB backbone is replaced with $–CF_2–$ (Fig. 1c, orange part) while the –O– is still linked to $CH_3–$ and $–CH_2–$ (Fig. 1c, light-blue part). As a result, the obtained FDMB molecule (Fig. 1c) is expected to be stable to both Li metal anodes and high-voltage cathodes. FDMB is an organic molecule that has never been reported; however, the ease of one-step synthesis and low costs of reagents endow FDMB with promise for large-scale commercialization (Supplementary Table 1 and Syntheses).

After the syntheses, the physicochemical properties of DMB and FDMB are determined: both show high boiling points (135 °C for DMB and 150 °C for FDMB; Supplementary Fig. 1). These solvents are further made into electrolytes with 1 M LiFSI salt, and they all (in the order of 1 M LiFSI/DME, 1 M LiFSI/DMB and 1 M LiFSI/FDMB hereafter) show high ion conductivities (21.9, 3.8, 3.5 mS cm^{-1}), high Li^+ transference numbers (0.39, 0.45, 0.48), low viscosities (0.58, 2.7, 5.0 cp), reasonable densities (0.966, 0.951, 1.25 g ml^{-1}) and low Li metal stripping/deposition overpotentials (~10, ~20, ~40 mV) (Supplementary Figs. 1–5). In particular, the 1 M LiFSI/FDMB is less flammable compared with the conventional carbonate electrolyte (Supplementary Video). Density functional theory (DFT) calculations show lower highest occupied molecular orbital levels for LiFSI/DMB and LiFSI/FDMB electrolytes compared with the DME case, corresponding semi-quantitatively to higher theoretical oxidation voltages[30] (5.48 V for LiFSI/DME, 5.52 V for LiFSI/DMB and 6.14 V for LiFSI/FDMB; Supplementary Fig. 6).

To experimentally verify the above-mentioned design principles, both high-voltage tolerance and Li metal CE are evaluated. Linear sweep voltammetry (LSV) measurements on Li|Al cells are conducted to determine the oxidation voltage (Fig. 1d). Unlike the low oxidation voltage of 1 M LiFSI/DME (~3.9 V)[23], 1 M LiFSI/DMB and 1 M LiFSI/FDMB show considerable high-voltage tolerance by giving oxidation voltages at ~5.2 V and >6 V, respectively. The potentiostatic polarization tests provide more accurate information on oxidation voltage, which is <4 V for 1 M LiFSI/DME, ~4.8 V for 1 M LiFSI/DMB and >5 V for 1 M LiFSI/FDMB (Supplementary Fig. 7). Scanning electron microscopy (SEM) images prove that Al foil remains intact in 1 M LiFSI/FDMB whereas it is corroded and cracked in DME or DMB electrolyte when holding at 5.5 V for three days (Supplementary Fig. 8).

The CEs of Li metal anodes are measured to confirm the cycling efficiency (Fig. 1e,f). 1 M LiFSI/DME is unstable with long-term cycling in Li|Cu half cells; however, the Li metal CE vastly improves when using 1 M LiFSI/DMB. Albeit still low for the initial few tens of cycles, the CE of 1 M LiFSI/DMB stabilizes at ~98.8% with cycling (Supplementary Fig. 9). By contrast, 1 M LiFSI/FDMB repeatably offers high first-cycle CE (~97.6%) and a rapid ramp-up to >99% within only five cycles (Fig. 1e and Supplementary Fig. 10), which is the fastest activation observed so far[13–15,17,22,31–33]. After this five-cycle activation, the CE maintains an average of 99.3% for over 300 cycles (Supplementary Fig. 9). Aurbach CE tests[34], which better evaluate the efficiency of Li cycling on a Li metal substrate, further prove the benefit of the FDMB design by showing a substantially improved CE (99.52%) compared with both DMB (97.7%) and DME (98.4%) (Fig. 1f and Supplementary Fig. 11). This CE is one of the highest among the state-of-the-art electrolytes[11,15,21,22]. The slightly higher overpotential shown in the FDMB cells (Fig. 1f and Supplementary Figs. 3 and 4) may be attributed to the moderate ion conductivity and high SEI resistance, as well as the densely packed Li morphology (that is low surface area)[35] in 1 M LiFSI/FDMB.

On the basis of the structure of FDMB, we further lengthen the carbon chain to synthesize fluorinated 1,5-dimethoxylpentane (FDMP, Syntheses) as the electrolyte solvent. As expected, high CE (~99%), fast activation (CE > 99% within two cycles) and oxidation stability (>6.5 V) are achieved with LiFSI/FDMP electrolytes (Supplementary Fig. 12), proving that our design principle can be expanded to a whole new family of solvent molecules.

Performance of practical Li metal batteries

The extraordinary Li metal performance along with high-voltage stability makes 1 M LiFSI/FDMB promising for practical Li metal batteries. Two types of Li metal battery are examined here: Li metal full cells with limited-excess Li, and anode-free pouch cells[36–39] (Fig. 2a). Both are considered as promising constructions for high-energy-density Li metal batteries. Figure 2b, c demonstrates Li metal battery performance where thin Li foils (50- and 20-μm thickness, 10- and 4-mAh-cm^{-2} capacity, respectively) are used as the limited-excess Li source. As shown in Fig. 2b, the cell capacity markedly decreases within 20 cycles when 1 M LiFSI/DME or the conventional electrolyte, 1 M $LiPF_6$ in ethylene carbonate/ethyl methyl carbonate (EC/EMC = 3/7) plus 2-wt% vinylene carbonate (VC), is used. By contrast, 1 M LiFSI/DMB prolongs the cycle life to ~50 cycles. Its high-voltage stability enables a better performance than DME, but the Li metal stability is still poor, showing notable capacity drop after 50 cycles. This can be further confirmed by its fast failure in Cu|NMC cells (Supplementary Fig. 13). In contrast, 1 M LiFSI/FDMB enables a 90% capacity retention even after 420 cycles with a high average CE of >99.98%. Moreover, this 1 M LiFSI/FDMB battery also survives several unexpected temperature fluctuations (Fig. 2b,c). This tolerance proves the robustness of 1 M LiFSI/FDMB. When the negative/positive capacity ratio is further reduced to ~2.5 and the electrolyte/cathode ratio is lowered to ~6 g Ah^{-1}, 1 M LiFSI/FDMB can still maintain stable battery cycling for >210 cycles (Fig. 2c). In addition to NMC532 batteries, 1 M LiFSI/FDMB maintains outstanding long-term cyclability and rate capability under other conditions such as NMC811 or LFP ($LiFePO_4$) cathodes, different cathode areal capacities, various limited-excess Li amounts and lean electrolyte (Supplementary Figs. 14–16).

Furthermore, aggressive anode-free pouch cells using 1 M LiFSI/FDMB are tested to realize high specific energy. Industrial dry pouch cells were purchased and directly tested after adding the electrolyte. The critical parameters such as total capacity (200–250 mAh), areal loading (~3–4 mAh cm^{-2}), active material content (~96%), electrolyte amount (~2 g Ah^{-1}), pressure (~250 kPa) and temperature (ambient, uncontrolled 18–25 °C) are all at practical

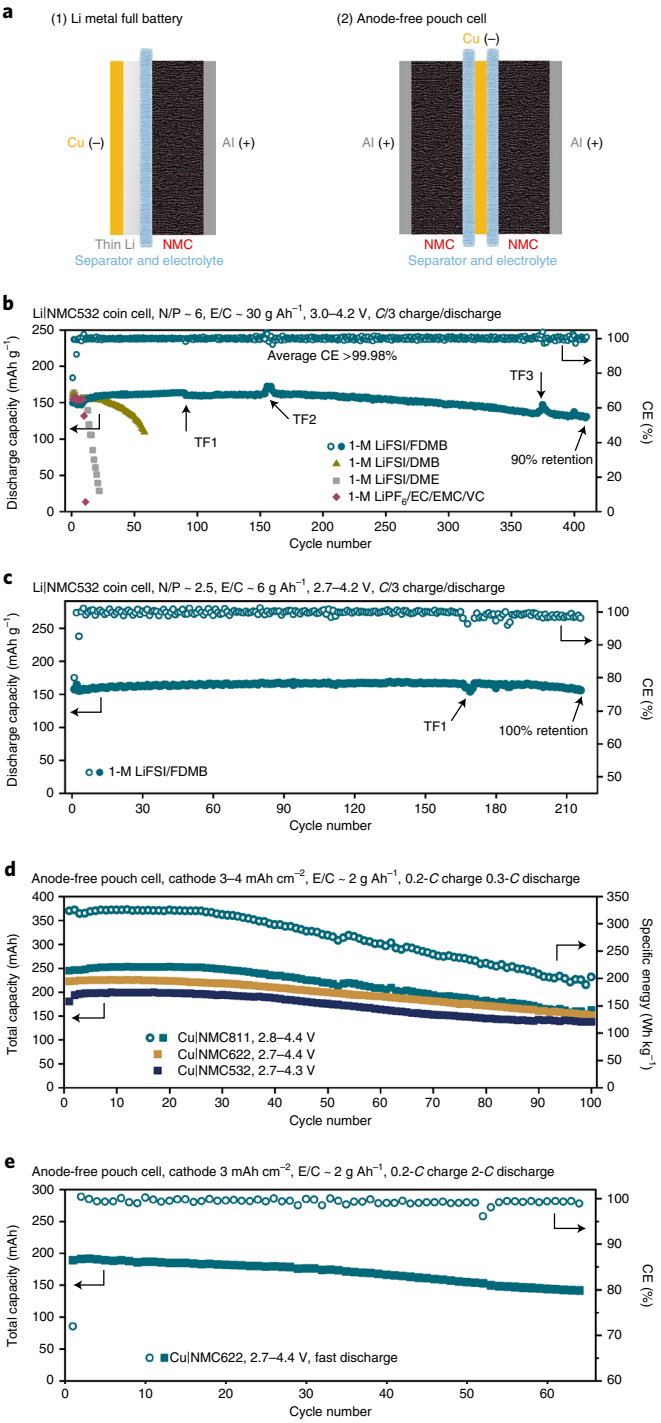

Fig. 2 | Li metal full battery performance. a, Configurations of practical Li metal batteries. **b**,**c**, Li metal full battery performance (50-μm Li in **b** and 20-μm Li in **c**) at room temperature. Before cycling at *C*/3, three precycles at *C*/10 were conducted. The average CE was calculated from the fifth to the final cycle. Temperature fluctuation (TF) 1, overcooled to ~18 °C; TF2 and TF3, cooling system failed for 2 d, resulting in temperature spike from room temperature to >40 °C, then back to room temperature. N/P, negative/positive capacity ratio; E/C, electrolyte/cathode ratio. **d**, Cycling performance of anode-free pouch cells at 0.2-*C* charge and 0.3-*C* discharge. The specific energy was calculated on the basis of the real mass of the whole pouch cell. **e**, Fast-discharge performance of the anode-free Cu|NMC622 pouch cell at 0.2-*C* charge and 2-*C* discharge.

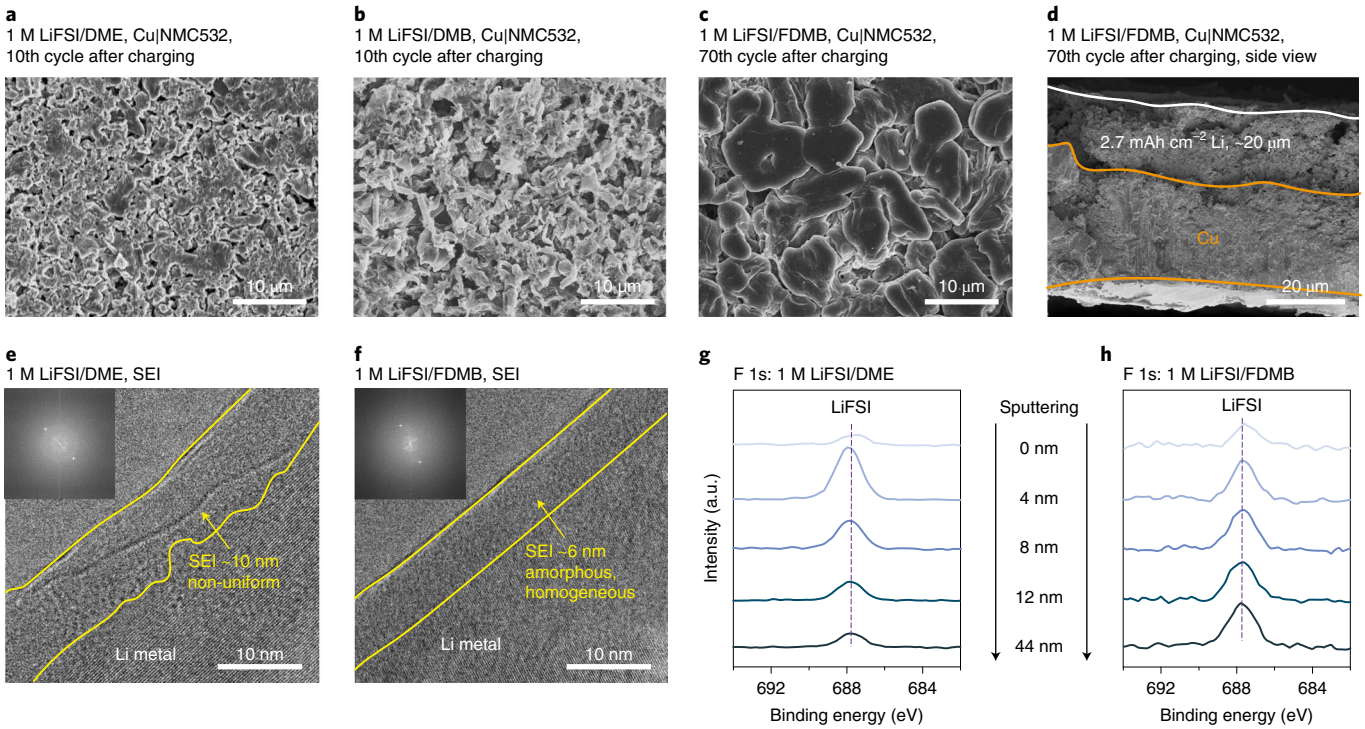

Fig. 3 | Li metal morphology and SEI. a–d, Li morphology in anode-free Cu|NMC532 (2.7 mAh cm^{-2}) coin cells using 1 M LiFSI/DME after 10 cycles (**a**), 1 M LiFSI/DMB after 10 cycles (**b**) and 1 M LiFSI/FDMB after 70 cycles (**c**,**d**). **e**,**f**, Cryo-TEM showing the SEIs of 1 M LiFSI/DME (**e**) and 1 M LiFSI/FDMB (**f**). Insets in **e** and **f**: the fast Fourier transforms of the SEIs. **g**,**h**, F 1s XPS depth profiles of Li metal surface in 1 M LiFSI/DME (**g**) and 1 M LiFSI/FDMB (**h**). a.u., arbitrary units.

levels[9,10] (Supplementary Table 2). Figure 2d shows the performance of the anode-free pouch cells. The Cu|NMC532 cell maintains its 80% capacity for 100 cycles, while the Cu|NMC622 ($LiNi_{0.6}Mn_{0.2}Co_{0.2}O_2$) and Cu|NM811 cells achieve 80 cycles and 70 cycles, respectively. It is worth noting that all cells were cycled with 100% depth of discharge, and this performance is one of the highest among the state-of-the-art anode-free cells (Supplementary Table 3). Additionally, the Cu|NMC811 cells exhibit a high specific energy of ~325 Wh kg^{-1}, determined from the total weight of the pouch. We believe that the specific energy can be further increased if single cells with higher total capacity (for example Ah-level cylinder or pouch cells) are investigated. To fulfil special battery applications, the fast-discharge capability of the Cu|NMC622 pouch cell is examined, and 80% capacity is retained after ~60 cycles (Fig. 2e). More anode-free coin or pouch cells are cycled under different conditions and they all show superior cycle life (Supplementary Figs. 13 and 17–19). For example, the home-made Cu|NMC811 pouch cell realizes 80% retention for over 90 cycles. The anode-free pouch cells maintain shiny and silver-coloured Li metal deposition even after 100 cycles, while generating little gas (Supplementary Fig. 20).

Li metal morphology and SEI structure

The Li metal deposition morphology and SEI nanostructure are carefully studied. When the 1 M LiFSI/DME or 1 M LiFSI/DMB is applied in Cu|NMC532 anode-free cells after 10 cycles, the Li structure on Cu is dendritic and porous (Fig. 3a,b and Supplementary Figs. 21–23). By contrast, with the 1 M LiFSI/FDMB electrolyte, the 2.7 mAh cm^{-2} Li deposited on Cu (~14 μm thick theoretically while ~20 μm observed) shows densely packed, flat, large grains even after 70 cycles (Fig. 3c,d and Supplementary Figs. 22 and 23). The morphology is highly beneficial to reducing the surface area for SEI growth as well as suppressing dead Li formation, leading to an ideal cycling performance[18,20,37]. The Li metal morphology of Li|NMC532 cells provides similar results as well (Supplementary Figs. 22 and 24).

Furthermore, cryo-TEM[40] is utilized to characterize the compact SEI[41] structure. In 1 M LiFSI/DME, the SEI layer is relatively thick (~10 nm) and non-uniform; however, an ultrathin (~6-nm) and amorphous SEI is observed on Li when 1 M LiFSI/FDMB is applied (Fig. 3e,f). Instead of containing wrinkles or non-uniform domains as does the SEI observed in 1 M LiFSI/DME or other conventional electrolytes[41–43], the SEI in 1 M LiFSI/FDMB exhibits extraordinary uniformity according to the fast Fourier transform (Fig. 3e,f insets). This is also one of the thinnest compact SEIs observed to date[11,40–43]. This feature can effectively reduce the Li consumption from SEI formation during each cycle, thus improving the CE[44]. Cryogenic energy dispersive X-ray spectroscopy shows that the SEI is rich in F, S and O, consistent with a heavily anion-derived SEI[11] (Supplementary Fig. 25). The F 1s spectra of X-ray photoelectron spectroscopy (XPS) conducted for the Li metal surface further support this argument (Fig. 3g,h). The peaks assigned to LiFSI (~688 eV) in 1 M LiFSI/FDMB have similar intensities throughout the depth profiling, indicating uniform SEI, while those in 1 M LiFSI/DME show large variation with sputtering. The XPS spectra of other elements and during Li|Li cell cycling are consistent with this conclusion (Supplementary Figs. 26 and 27). Albeit thin and uniform for the compact SEI, ion-insulating species such as LiFSI, $-SO_x$ and Li_2S_x, which correlate with the high SEI resistance, are detected by XPS on the Li surface in 1 M LiFSI/FDMB (Supplementary Figs. 26 and 27). However, the SEI resistance in 1 M LiFSI/FDMB gradually stabilizes with resting while that in DME or DMB continuously grows (Supplementary Fig. 4). These results indicate that the SEI formed in 1 M LiFSI/FDMB not only is more anion derived but also self-passivates and provides better protection for Li metal anodes over time.

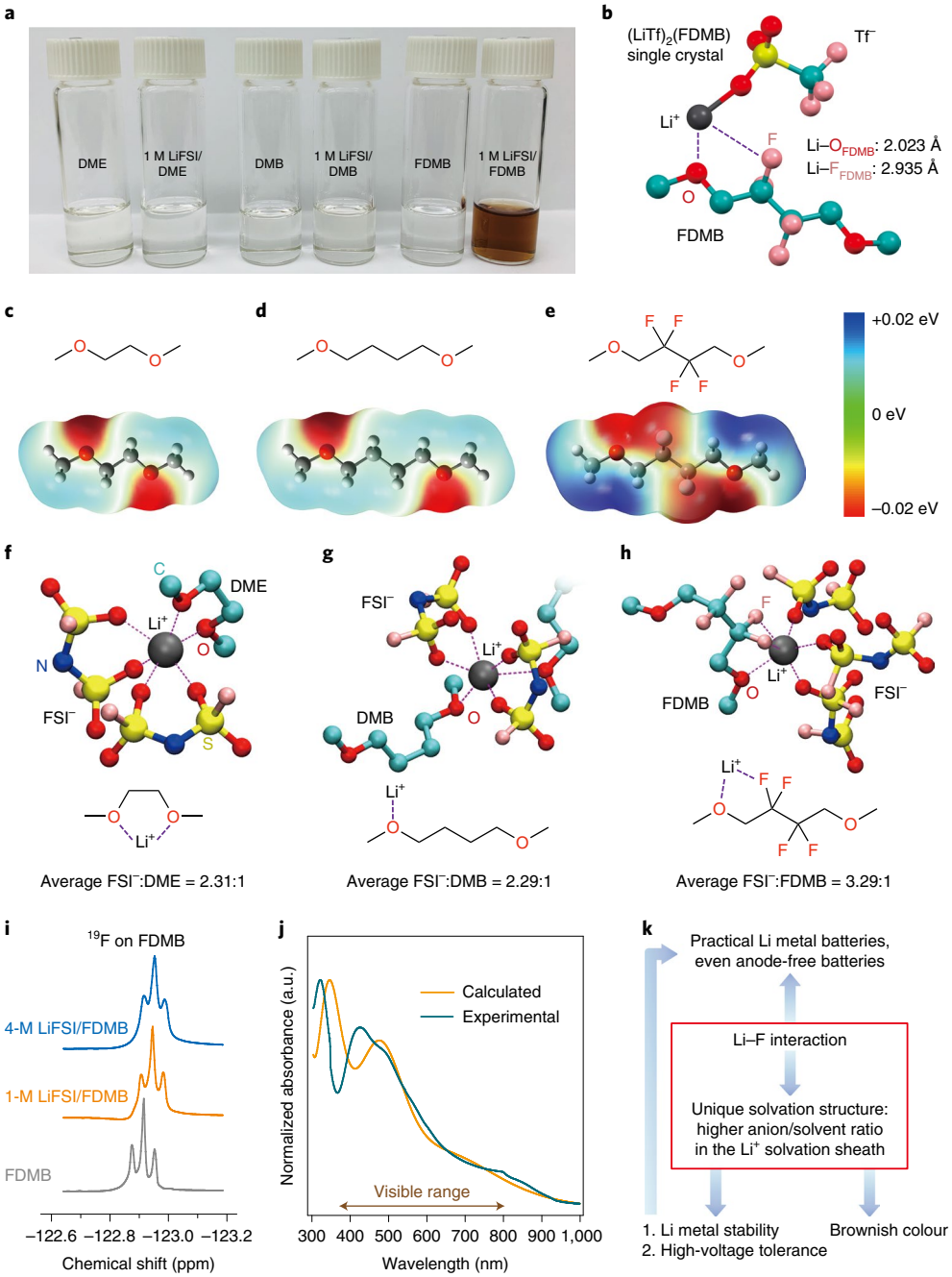

Fig. 4 | Unique solvation structure in 1 M LiFSI/FDMB. a, Optical image of three liquids and their 1 M LiFSI electrolytes. **b**, Single crystal of LiTf/FDMB showing Li–F interactions. For clarity, only one LiTf and one FDMB are shown. **c**–**e**, ESP comparison of DME (**c**), DMB (**d**) and FDMB (**e**). **f**–**h**, Solvation structure of 1 M LiFSI/DME (**f**), 1 M LiFSI/DMB (**g**) and 1 M LiFSI/FDMB (**h**) given by MD simulations and the corresponding average ratio of solvation bindings from FSI^- anions to those from solvents in the solvation sheath. **i**, ^{19}F-NMR of LiFSI/FDMB electrolytes. **j**, Ultraviolet–visible spectra of 1 M LiFSI/FDMB. **k**, Logic flow of the structure–property relationship of 1 M LiFSI/FDMB: the Li–F interaction and high anion/solvent ratio in the Li^+ solvation sheath result in the unconventional colour and stabilize both the Li metal and the high-voltage cathode, further enabling Li metal full batteries. Colour scheme in **b**,**f**–**h**: dark grey, Li; pink, F; red, O; light blue, C; navy, N; yellow, S. For clarity, H atoms are not shown in **b**,**f**–**h**.

Li–F interaction and solvation structure

The electrolyte chemistry is studied to provide a better understanding of the performance and SEI formation. Unlike typical transparent and colourless electrolytes, 1 M LiFSI/FDMB is brownish in colour (Fig. 4a and Supplementary Fig. 28). The NMR study rules out the possibility of impurity or decomposition (Supplementary Fig. 29). In addition, when Li salts with other anions are dissolved in FDMB, they all show similar colours; nevertheless, when Na or K salts or ionic liquids are dissolved, only colourless solutions are obtained (Supplementary Fig. 30). These tests indicate that there are some unique Li^+–solvent interactions in 1 M LiFSI/FDMB.

To check the coordination structure, a single crystal of lithium triflate (LiTf) cocrystallized with FDMB was obtained (Fig. 4b, Single crystals and Crystallographic Data 1). LiTf is chosen because it is structurally similar to LiFSI yet much easier to crystallize.

The crystal structure demonstrates that the Li–F_{FDMB} (2.935 Å) distance is similar to that of Li–O_{FDMB} (2.023 Å), thereby indicating a weak yet existing interaction between Li^+ ions and F atoms on FDMB[45]. This Li–F interaction can be rationalized by the electrostatic potential (ESP) calculations, which strongly correlate with non-covalent interactions[46] (Fig. 4c–e). The isopotential surfaces of DME and DMB show similar trends, where the negative parts only concentrate on O atoms. Nevertheless, the isopotential surface of FDMB is completely different: the negative charge is almost equally located at both O_{FDMB} and F_{FDMB} atoms and contributes to the coordination with positive Li^+.

Molecular dynamics (MD) simulations are conducted to further corroborate the coordination structures (Fig. 4f–h). The DME molecule coordinates with the Li^+ ion like a 'clamp' with both its –O– groups (Fig. 4f and Supplementary Fig. 31). Such a coordination geometry is well known in both liquid[47] or polymer[48] electrolyte systems and single crystals[49]. For DMB, the majority of Li^+–solvent coordination structures are 'linear', where only one –O– group on DMB is bound with one Li^+ ion (Fig. 4g and Crystallographic Data 2); however, the clamp coordination can still be found as a minority (Supplementary Fig. 32). Different from either DME or DMB, a five-member ring structure is observed in LiFSI/FDMB where the Li^+ ion is bound simultaneously with O_{FDMB} and F_{FDMB} atoms (Fig. 4h and Supplementary Fig. 33). This coordination matches well with the above-mentioned single-crystal result, and can be further cross-validated by simulated radial distribution functions (Supplementary Fig. 34), Fourier-transform infrared spectra (Supplementary Fig. 35) and ^{19}F-NMR (Fig. 4i). With the LiFSI concentration increasing, the ^{19}F peak on FDMB shows an upfield shift, indicating Li–F interaction[18]. The measured ultraviolet–visible spectrum of 1 M LiFSI/FDMB matches well with the calculated one, where the broad absorption in the visible range causes the brownish colour (Fig. 4j and Supplementary Fig. 36).

Finally, the difference in coordination leads to non-negligible differences in the Li^+ solvation sheath. The average ratio of solvation bindings from FSI^- anions to those from solvent (coordination provided by FSI^- anions and solvent surrounding one Li^+ ion) is 2.31:1 for DME and 2.29:1 for DMB, respectively (Fig. 4f,g). Nevertheless, the FSI^-/solvent ratio in the Li^+ solvation sheath is vastly increased, to 3.29:1, in 1 M LiFSI/FDMB (Fig. 4h), which suggests that FDMB performs poorly in dissociating ion pairs despite its contribution from Li–F interaction. The uncoordinated ether band (that is free solvent) dominates in the Fourier-transform infrared spectra of 1 M LiFSI/FDMB (Supplementary Fig. 35), proving the weak solvation ability of FDMB. This argument is also consistent with the ^{7}Li-NMR, where the peak of 1 M LiFSI/FDMB is shifted upfield, which is an indication of better anion shielding effect (Supplementary Fig. 37). With more anions participating in the Li^+ solvation, 1 M LiFSI/FDMB is expected to mitigate harmful parasitic reactions on Li metal anodes[11,18–22,50]. This is consistent with the ultrathin SEI observed by cryo-TEM and the evenly distributed SEI composition with XPS depth profiling. Meanwhile, FSI^- anions are tightly bound in such a solvation environment, so Al corrosion caused by FSI^- can be suppressed[19,51] (Supplementary Fig. 8), thus showing higher oxidation stability for 1 M LiFSI/FDMB. In summary, the Li–F interaction and special solvation structure in the 1 M LiFSI/FDMB electrolyte not only result in the unconventional electrolyte colour but also greatly stabilize both Li metal and cathode, further leading to excellent performance in Li metal full batteries (Fig. 4k).

Conclusions

In this work, a low-concentration, additive-free electrolyte is developed using a rationally designed solvent molecule, FDMB, solely as the solvent, and LiFSI as the single salt. A unique Li–F interaction is observed in 1 M LiFSI/FDMB. This coordination further leads to higher anion content in the Li^+ solvation sheath, endowing the electrolyte simultaneously with Li metal compatibility and high-voltage stability. Therefore, 1 M LiFSI/FDMB promises a high CE (99.52%) with fast activation (>99% within five cycles) in Li|Cu half cells, and >6 V oxidative stability. A thin SEI layer (~6 nm) is observed by cryo-TEM while favourable densely packed Li morphology is shown by SEM in Cu|NMC cells after long-term cycling. Furthermore, over 420 cycles for a limited-excess Li|NMC full cell are achieved with an average CE of 99.98%, during which even several temperature fluctuations are overcome. Industrial hundreds-of-mAh Cu|NMC532 pouch cells are found to maintain 80% capacity retention for 100 cycles, while the Cu|NMC811 ones exhibit a high single-cell specific energy of ~325 Wh kg^{-1}. The molecular design concept in this work provides a new direction for electrolyte engineering.

Methods

Materials. 2,2,3,3-Tetrafluoro-1,4-butanediol was purchased from SynQuest. 1,4-Butanediol, methyl iodide, sodium hydride (60% in mineral oil) and other general reagents were purchased from Sigma-Aldrich or Fisher Scientific. All chemicals were used without further purification. LiFSI was purchased from Oakwood and Fluolyte; LiTFSI was provided by Solvay; LiTf, VC and fluoroethylene carbonate were purchased from Sigma-Aldrich. DME (99.5% over molecular sieves) was purchased from Acros. The 1 M $LiPF_6$ in EC/EMC (LP57), 1 M $LiPF_6$ in EC/DMC (dimethyl carbonate) (LP30) and 1 M $LiPF_6$ in EC/DEC (diethyl carbonate) (LP40) were purchased from Gotion. The commercial Li battery separator Celgard 2325 (25 µm thick, polypropylene/polyethylene/polypropylene) was purchased from Celgard and used in all coin cells. Thick Li foil (~750 µm thick) and Cu current collector (25 µm thick) were purchased from Alfa Aesar. Thin Li foils (~50 µm and ~20 µm thick) were provided by Hydro-Québec. Commercial LFP and NMC532 cathode sheets were purchased from MTI, and NMC811 cathode sheets were purchased from Targray (~2-mAh-cm^{-2} areal capacity for all sheets). Industrial dry Cu|NMC532, Cu|NMC622 and Cu|NMC811 pouch cells were purchased from Hunan Li-Fun Technology. Other battery materials, such as 2032-type coin-cell cases, springs and spacers, were all purchased from MTI.

Syntheses. DMB (Supplementary Figs. 40–42): To a round-bottom flask were added dry tetrahydrofuran (THF) and 1,4-butanediol. The solution was cooled to 0 °C and then 2.5 equivalents of sodium hydride were added slowly. Bubbling was observed upon sodium hydride addition. Then, 2.5 equivalents of methyl iodide were added dropwise to the stirring suspension followed by heating to reflux overnight. The mixture was then filtered off and the solvents were removed under vacuum. The crude sample was vacuum distilled to yield the final product as a colourless liquid. The product was then filtered off through a 0.45-µm polytetrafluoroethylene filter and moved to an argon glovebox for further use. Yield: 76%. ^{1}H-NMR (400 MHz, d^6-DMSO, δ/ppm): 3.30–3.27 (m, 4 H), 3.20 (s, 6 H), 1.51–1.48 (m, 4 H). ^{13}C-NMR (100 MHz, d^6-DMSO, δ/ppm): 72.36, 58.37, 26.50.

FDMB (Supplementary Figs. 43–46): The same procedure as for DMB synthesis was used, except that 1,4-butanediol was changed to 2,2,3,3-tetrafluoro-1,4-butanediol. Yield: 85%. ^{1}H-NMR (400 MHz, d^8-THF, δ/ppm): 3.85–3.76 (m, 4 H), 3.42 (s, 6 H). ^{13}C-NMR (100 MHz, d^8-THF, δ/ppm): 119.09–114.06, 69.54–69.02, 59.48. ^{19}F-NMR (376 MHz, d^8-THF, δ/ppm): –123.50 to –123.58 (m, 4 F).

FDMP (Supplementary Figs. 47–50): The same procedure as for DMB synthesis was used, except that 1,4-butanediol was changed to 2,2,3,3,4,4-hexafluoro-1,5-pentanediol. Yield: 89%. ^{1}H-NMR (400 MHz, d^8-THF, δ/ppm): 3.92–3.84 (m, 4 H), 3.43 (s, 6 H). ^{13}C-NMR (100 MHz, d^8-THF, δ/ppm): 119.02–108.86, 69.31–68.79, 59.56. ^{19}F-NMR (376 MHz, d^8-THF, δ/ppm): –121.44 to –121.52 (m, 4 F), –127.66 (s, 2 F).

Electrolytes. All the electrolytes were made and stored in argon-filled glovebox (Vigor, oxygen <0.01 ppm, water <0.01 ppm). LiFSI (1,122 mg) or LiTFSI (1,722 mg) was dissolved and stirred in 6 ml DME, DMB or FDMB to obtain 1 M LiFSI/DME, 1 M LiFSI/DMB, 1 M LiFSI/FDMB, 1 M LiTFSI/DME, 1 M LiTFSI/DMB or 1 M LiTFSI/FDMB, respectively. The LP57 with 2-wt% VC and LP30 were used as control electrolytes.

Theoretical calculations. DFT: The molecular geometries for the ground states were optimized by DFT at the B3LYP/6–311G + (d, p) level, and then the energy, orbital levels and ESPs of molecules were evaluated at the B3LYP/6–311G + (d, p) level as well. All the DFT calculations were carried out with the Gaussian 09 package.

MD simulations: Molecules and ions were described by the optimized potentials for a liquid simulations all-atom (OPLS-AA)[52] force field. Partial charges on solvent (that is DME, DMB and FDMB) atoms were computed by fitting the molecular ESP at the atomic centres with the Møller–Plesset

second-order perturbation method with the correlation-consistent polarized valence cc-pVTZ(-f) basis set[53]. The simulation boxes were cubic with a side length of about 6 nm and contained 1 M LiFSI solvated in different solvents. During simulations, the temperature was controlled at 300 K using a Nosé–Hoover thermostat with a relaxation time of 0.2 ps and the pressure was controlled at 1 bar using a Parrinello–Rahman barostat with a relaxation time of 2.0 ps. All MD simulations were conducted with the GROMACS 2018 program[54] for 50 ns, and the last 20 ns were used for analysis. Li^+ ion solvation structures were analysed with a self-written script based on the MDAnalysis Python module[55].

Material characterizations. ^{1}H-, ^{13}C- and ^{19}F-NMR spectra were recorded on a Varian Mercury 400-MHz NMR spectrometer and ^{7}Li-NMR spectra were recorded on a UI 300-MHz NMR spectrometer at room temperature. Fourier-transform infrared spectra were measured using a Nicolet iS50 with a diamond attenuated total reflectance attachment. An FEI Titan 80–300 environmental (scanning) transmission electron microscope and a Gatan 626 holder were used for cryo-TEM experiments. Cryo-TEM sample preparations prevent air reaction and beam damage, as described previously[40,42,43]. Low-dose electron exposure procedures were employed using a Gatan OneView complementary metal–oxide–semiconductor camera, with 1,000-e^--Å^2 total dosage. The transmission electron microscope is equipped with an aberration corrector in the image-forming lens, which was tuned before imaging. An FEI Magellan 400 XHR scanning electron microscope was used for SEM and energy-dispersive X-ray spectroscopy characterizations. A Bruker D8 Venture X-ray diffractometer was used for single-crystal data collection. For XPS measurements, each Li foil (soaked in the electrolyte for 4 d or after Li|Li cell cycling) was washed with the corresponding solvent for 30 s to remove the remaining electrolyte. The samples were transferred and sealed into the XPS holder in the argon-filled glovebox. The XPS profiles were collected with a PHI VersaProbe 1 scanning XPS microprobe. Viscosity measurements were carried out using an Ares G2 rheometer (TA Instruments) with an advanced Peltier system at 25 °C. A Karl-Fisher titrator was used to determine the water content in electrolytes. Ultraviolet–visible spectra were collected using an Agilent Cary 6000i ultraviolet–visible–near-infrared instrument.

Electrochemical measurements. All battery components used in this work were commercially available and all electrochemical tests were carried out in a Swagelok-cell, 2032-type coin-cell or pouch-cell configuration. All cells were fabricated in an argon-filled glovebox, and one layer of Celgard 2325 was used as a separator. Electrochemical impedance spectroscopy, Li^+ transference number (LTN), LSV and pouch-cell cycling were carried out on a Biologic VMP3 system. The cycling tests for coin cells were carried out on an Arbin system or Land instrument. The electrochemical impedance spectroscopy measurements were taken over a frequency range of 7 MHz to 100 mHz. For the LTN measurements, 10-mV constant voltage bias was applied to Li|Li cells. The anodic constant-voltage tests were carried out over a voltage range of –0.1 to 2 V for three cycles in Li|Cu cells, while the cathodic LSV tests were over a voltage range of 2.5 to 7 V. For Li|Cu half-cell CE cycling tests, ten precycles between 0 and 1 V were initialized to clean the Cu electrode surface, and then cycling was done by depositing 1 (or 0.5) mAh cm^{-2} of Li onto the Cu electrode followed by stripping to 1 V. The average CE is calculated by dividing the total stripping capacity by the total deposition capacity after the formation cycle. For the Aurbach CE test[34], a standard protocol was followed: (1) perform one initial formation cycle with Li deposition of 5 mAh cm^{-2} on Cu under 0.5-mA-cm^{-2} current density and stripping to 1 V; (2) deposit 5-mAh-cm^{-2} Li on Cu under 0.5 mA cm^{-2} as a Li reservoir; (3) repeatedly strip/deposit Li of 1 mAh cm^{-2} under 0.5 mA cm^{-2} for 10 cycles; (4) strip all Li to 1 V. The Li|NMC and Cu|NMC full cells were cycled with the following method (unless specially listed): after the first two activation cycles at *C*/10 charge/discharge (or 0.1-*C* charge 0.3-*C* discharge for anode-free pouch cells), the cells were cycled at different rates. Then a constant-current–constant-voltage protocol was used for cycling: cells were charged to top voltage and then held at that voltage until the current dropped below *C*/20. The NMC532 coin cells were cycled between 2.7 and 4.2 V or 3.0 and 4.2 V; the NMC532 pouch cells were cycled between 2.7 and 4.2 V or 2.7 and 4.3 V; the NMC622 pouch cells were cycled between 2.7 and 4.4 V; the NMC811 coin cells were cycled between 2.8 and 4.4 V; the NMC811 pouch cells were cycled between 2.8 and 4.4 V or 3.0 and 4.4 V. For anode-free pouch cells, the current was tuned to guarantee the cycling time. All cells were cycled under ambient conditions without temperature control.

Single crystals. LiTf/FDMB (Crystallographic Data 1 and Supplementary Fig. 51): Anhydrous LiTf was predried at 110 °C in an argon-filled glovebox for 3 d. LiTf (0.3 mg) was added to 200 µl FDMB and the suspension was sonicated until a coloured solution formed. The solution was left undisturbed and open capped in the glovebox for over a week to obtain coloured flake-like crystals. A suitable crystal was selected and mounted on a Bruker D8 Venture diffractometer. The crystal was kept at 100 K during data collection. Using Olex2 (ref. [56]), the structure was solved with the SIR2014 (ref. [57]) structure solution program using Direct Methods and refined with the SHELXL[58,59] refinement package using least-squares minimization. Crystallographic data of LiTf/FDMB have been submitted to the Cambridge Crystallographic Database (reference number CCDC 1935863).

LiTf/DMB (Crystallographic Data 2 and Supplementary Fig. 52): The same crystal growth method as for LiTf/FDMB was used except that 0.1 mg LiTf was dissolved in 200 µl DMB. The obtained crystals were colourless and needle-like. Crystallographic data of LiTf/DMB have been submitted to the Cambridge Crystallographic Database (reference number CCDC 1945342). Crystallographic data are available free of charge at http://www.ccdc.cam.ac.uk/data_request/cif.

Data availability

All relevant data are included in the paper and its Supplementary Information.

Code availability

The Python script for analysing the Li^+ solvation structure is available at https://github.com/xianshine/LiSolvationStructure.git.

Received: 12 December 2019; Accepted: 14 May 2020;
Published online: 22 June 2020

References

1. Press release: The Nobel Prize in Chemistry 2019. *The Nobel Prize* https://www.nobelprize.org/prizes/chemistry/2019/press-release/ (2019).
2. Battery revolution to evolution. *Nat. Energy* **4**, 893 (2019).
3. Janek, J. & Zeier, W. G. A solid future for battery development. *Nat. Energy* **1**, 16141 (2016).
4. Lin, D., Liu, Y. & Cui, Y. Reviving the lithium metal anode for high-energy batteries. *Nat. Nanotechnol.* **12**, 194–206 (2017).
5. Albertus, P., Babinec, S., Litzelman, S. & Newman, A. Status and challenges in enabling the lithium metal electrode for high-energy and low-cost rechargeable batteries. *Nat. Energy* **3**, 16–21 (2018).
6. Choi, J. W. & Aurbach, D. Promise and reality of post-lithium-ion batteries with high energy densities. *Nat. Rev. Mater.* **1**, 16013 (2016).
7. Xu, K. Electrolytes and interphases in Li-ion batteries and beyond. *Chem. Rev.* **114**, 11503–11618 (2014).
8. Liu, B., Zhang, J. & Xu, W. Advancing lithium metal batteries. *Joule* **2**, 833–845 (2018).
9. Liu, J. et al. Pathways for practical high-energy long-cycling lithium metal batteries. *Nat. Energy* **4**, 180–186 (2019).
10. Cao, Y., Li, M., Lu, J., Liu, J. & Amine, K. Bridging the academic and industrial metrics for next-generation practical batteries. *Nat. Nanotechnol.* **14**, 200–207 (2019).
11. Cao, X. et al. Monolithic solid–electrolyte interphases formed in fluorinated orthoformate-based electrolytes minimize Li depletion and pulverization. *Nat. Energy* **4**, 796–805 (2019).
12. Liu, Y. et al. Solubility-mediated sustained release enabling nitrate additive in carbonate electrolytes for stable lithium metal anode. *Nat. Commun.* **9**, 3656 (2018).
13. Fan, X. et al. Non-flammable electrolyte enables Li-metal batteries with aggressive cathode chemistries. *Nat. Nanotechnol.* **13**, 715–722 (2018).
14. Fan, X. et al. All-temperature batteries enabled by fluorinated electrolytes with non-polar solvents. *Nat. Energy* **4**, 882–890 (2019).
15. Yang, Y. et al. High-efficiency lithium-metal anode enabled by liquefied gas electrolytes. *Joule* **3**, 1986–2000 (2019).
16. Yamada, Y., Wang, J., Ko, S., Watanabe, E. & Yamada, A. Advances and issues in developing salt-concentrated battery electrolytes. *Nat. Energy* **4**, 269–280 (2019).
17. Fan, X. et al. Highly fluorinated interphases enable high-voltage Li-metal batteries. *Chem* **4**, 174–185 (2018).
18. Ren, X. et al. Enabling high-voltage lithium-metal batteries under practical conditions. *Joule* **3**, 1662–1676 (2019).
19. Ren, X. et al. Localized high-concentration sulfone electrolytes for high-efficiency lithium-metal batteries. *Chem* **4**, 1877–1892 (2018).
20. Niu, C. et al. High-energy lithium metal pouch cells with limited anode swelling and long stable cycles. *Nat. Energy* **4**, 551–559 (2019).
21. Chen, S. et al. High-efficiency lithium metal batteries with fire-retardant electrolytes. *Joule* **2**, 1548–1558 (2018).
22. Chen, S. et al. High-voltage lithium-metal batteries enabled by localized high-concentration electrolytes. *Adv. Mater.* **30**, 1706102 (2018).
23. Qian, J. et al. High rate and stable cycling of lithium metal anode. *Nat. Commun.* **6**, 6362 (2015).
24. Amanchukwu, C. V. et al. A new class of ionically conducting fluorinated ether electrolytes with high electrochemical stability. *J. Am. Chem. Soc.* **142**, 7393–7403 (2020).
25. Jiao, S. et al. Stable cycling of high-voltage lithium metal batteries in ether electrolytes. *Nat. Energy* **3**, 739–746 (2018).
26. Li, N., Leng, Y., Hickner, M. A. & Wang, C. Y. Highly stable, anion conductive, comb-shaped copolymers for alkaline fuel cells. *J. Am. Chem. Soc.* **135**, 10124–10133 (2013).

27. Zhang, X., Sheng, L., Higashihara, T. & Ueda, M. Polymer electrolyte membranes based on poly(*m*-phenylene)s with sulfonic acid *via* long alkyl side chains. *Polym. Chem.* **4**, 1235–1242 (2013).
28. Li, T., Zhang, X.-Q., Shi, P. & Zhang, Q. Fluorinated solid-electrolyte interphase in high-voltage lithium metal batteries. *Joule* **3**, 2647–2661 (2019).
29. Aspern, N., Röschenthaler, G.-V., Winter, M. & Cekic-Laskovic, I. Fluorine and lithium: ideal partners for high-performance rechargeable battery electrolytes. *Angew. Chem. Int. Ed.* **58**, 15978–16000 (2019).
30. Zhang, Z. et al. Fluorinated electrolytes for 5 V lithium-ion battery chemistry. *Energy Environ. Sci.* **6**, 1806–1810 (2013).
31. Zeng, Z. et al. Non-flammable electrolytes with high salt-to-solvent ratios for Li-ion and Li-metal batteries. *Nat. Energy* **3**, 674–681 (2018).
32. Suo, L. et al. Fluorine-donating electrolytes enable highly reversible 5-V-class Li metal batteries. *Proc. Natl Acad. Sci. USA* **115**, 1156–1161 (2018).
33. Xue, W. et al. FSI-inspired solvent and "full fluorosulfonyl" electrolyte for 4 V class lithium-metal batteries. *Energy Environ. Sci.* **13**, 212–220 (2020).
34. Adams, B. D., Zheng, J., Ren, X., Xu, W. & Zhang, J.-G. Accurate determination of Coulombic efficiency for lithium metal anodes and lithium metal batteries. *Adv. Energy Mater.* **8**, 1702097 (2018).
35. Liu, Y. et al. An artificial solid electrolyte interphase with high Li-ion conductivity, mechanical strength, and flexibility for stable lithium metal anodes. *Adv. Mater.* **29**, 1605531 (2017).
36. Zhang, J. G. Anode-less. *Nat. Energy* **4**, 637–638 (2019).
37. Weber, R. et al. Long cycle life and dendrite-free lithium morphology in anode-free lithium pouch cells enabled by a dual-salt liquid electrolyte. *Nat. Energy* **4**, 683–689 (2019).
38. Genovese, M. et al. Hot formation for improved low temperature cycling of anode-free lithium metal batteries. *J. Electrochem. Soc.* **166**, A3342–A3347 (2019).
39. Nanda, S., Gupta, A. & Manthiram, A. Anode-free full cells: a pathway to high-energy density lithium-metal batteries. *Adv. Energy Mater.* 2000804 (2020). https://doi.org/10.1002/aenm.202000804
40. Li, Y. et al. Atomic structure of sensitive battery materials and interfaces revealed by cryo–electron microscopy. *Science* **358**, 506–510 (2017).
41. Huang, W., Wang, H., Boyle, D. T., Li, Y. & Cui, Y. Resolving nanoscopic and mesoscopic heterogeneity of fluorinated species in battery solid-electrolyte interphases by cryogenic electron microscopy. *ACS Energy Lett.* **5**, 1128–1135 (2020).
42. Wang, J. et al. Improving cyclability of Li metal batteries at elevated temperatures and its origin revealed by cryo-electron microscopy. *Nat. Energy* **4**, 664–670 (2019).
43. Li, Y. et al. Correlating structure and function of battery interphases at atomic resolution using cryoelectron microscopy. *Joule* **2**, 2167–2177 (2018).
44. Fang, C. et al. Quantifying inactive lithium in lithium metal batteries. *Nature* **572**, 511–515 (2019).
45. Yu, Z. et al. A dynamic, electrolyte-blocking, and single-ion-conductive network for stable lithium-metal anodes. *Joule* **3**, 2761–2776 (2019).
46. Dou, J.-H. et al. Organic semiconducting alloys with tunable energy levels. *J. Am. Chem. Soc.* **141**, 6561–6568 (2019).
47. Ren, X. et al. High-concentration ether electrolytes for stable high-voltage lithium metal batteries. *ACS Energy Lett.* **4**, 896–902 (2019).
48. Mackanic, D. G. et al. Crosslinked poly(tetrahydrofuran) as a loosely coordinating polymer electrolyte. *Adv. Energy Mater.* **8**, 1800703 (2018).
49. Henderson, W. A., Brooks, N. R. & Smyrl, W. H. Polymeric $[Li(NO_3)(monoglyme)]_n$. *Acta Crystallogr. E* **58**, m500–m501 (2002).
50. Wang, Z. et al. An anion-tuned solid electrolyte interphase with fast ion transfer kinetics for stable lithium anodes. *Adv. Energy Mater.* **10**, 1903843 (2020).
51. Zhang, C. et al. Chelate effects in glyme/lithium bis(trifluoromethanesulfonyl) amide solvate ionic liquids, part 2: Importance of solvate-structure stability for electrolytes of lithium batteries. *J. Phys. Chem. C* **118**, 17362–17373 (2014).
52. Jorgensen, W. L., Maxwell, D. S. & Tirado-Rives, J. Development and testing of the OPLS all-atom force field on conformational energetics and properties of organic liquids. *J. Am. Chem. Soc.* **118**, 11225–11236 (1996).
53. Sambasivarao, S. V. & Acevedo, O. Development of OPLS-AA force field parameters for 68 unique ionic liquids. *J. Chem. Theory Comput.* **5**, 1038–1050 (2009).
54. Abraham, M. J. et al. GROMACS: high performance molecular simulations through multi-level parallelism from laptops to supercomputers. *SoftwareX* **1–2**, 19–25 (2015).
55. Michaud-Agrawal, N., Denning, E. J., Woolf, T. B. & Beckstein, O. MDAnalysis: a toolkit for the analysis of molecular dynamics simulations. *J. Comput. Chem.* **32**, 2319–2327 (2011).
56. Dolomanov, O. V., Bourhis, L. J., Gildea, R. J., Howard, J. A. K. & Puschmann, H. OLEX2: a complete structure solution, refinement and analysis program. *J. Appl. Crystallogr.* **42**, 339–341 (2009).
57. Burla, M. C. et al. Crystal structure determination and refinement via SIR2014. *J. Appl. Crystallogr.* **48**, 306–309 (2015).
58. Sheldrick, G. M. SHELXT—integrated space-group and crystal-structure determination. *Acta Crystallogr. A* **71**, 3–8 (2015).
59. Sheldrick, G. M. Crystal structure refinement with SHELXL. *Acta Crystallogr. C* **71**, 3–8 (2015).

Acknowledgements

This work is supported by the US Department of Energy, under the Assistant Secretary for Energy Efficiency and Renewable Energy, Office of Vehicle Technologies, Battery Materials Research (BMR) Program, and by the Battery 500 Consortium. Part of this work was performed at the Stanford Nano Shared Facilities, supported by the National Science Foundation under award ECCS-1542152. Z.Y. thanks X. Xu from Hunan Li-Fun Technology for fabricating pouch cells, Beijing Golden Feather New Energy Technology for providing LiFSI and Z. Yao for discussion on the DFT calculations. All authors thank K. Zaghib from Hydro-Québec for preparing and providing the thin Li metal foils. D.G.M. acknowledges support by the National Science Foundation Graduate Research Fellowship Program under grant no. (DGE-114747). C.V.A. acknowledges the TomKat Center Postdoctoral Fellowship in Sustainable Energy for funding support.

Author contributions

Z.Y., H.W., Y.C. and Z.B. conceived the idea. Z.Y. and H.W. designed the experiments. Y.C. and Z.B. directed the project. Z.Y. performed the syntheses, material characterizations, DFT calculations, electrochemical measurements and coin-cell tests. H.W. performed the XPS measurements, pouch-cell fabrication and tests, and coin-cell tests. X.K. and J.Q. conducted the MD simulations and rationales. William Huang performed the cryo-TEM and cryogenic energy-dispersive X-ray spectroscopy measurements. Y.T., William Huang and E.G.L. performed the SEM experiments. K.W. and X.W. helped with the single-crystal measurement and structure refinement. D.G.M. and C.V.A. collected the ^{7}Li-NMR spectra. Wenxiao Huang helped with the pouch-cell fabrication and tests. S.C. measured the viscosities. Y.Z. collected the ultraviolet–visible spectra. S.T.H. measured the water contents. Y.M. helped with the syntheses. All authors discussed and analysed the data. Z.Y., H.W., Y.C. and Z.B. wrote and revised the manuscript.

Competing interests

This work has been filed as US Provisional Patent Application No. 62/928,638.

Additional information

Supplementary information is available for this paper at https://doi.org/10.1038/s41560-020-0634-5.

Correspondence and requests for materials should be addressed to Y.C. or Z.B.

Reprints and permissions information is available at www.nature.com/reprints.

Publisher's note Springer Nature remains neutral with regard to jurisdictional claims in published maps and institutional affiliations.